A Numerical Study on Cavitations in Nonlinear Elasticity — Defects and Configurational Forces*

Yijiang Lian and Zhiping Li†

LMAM & School of Mathematical Sciences,
Peking University, Beijing 100871, China

Abstract

An iso-parametric finite element method is introduced in this paper to study cavitations and configurational forces in nonlinear elasticity. The method is shown to be highly efficient in capturing the cavitation phenomenon, especially in dealing with multiple cavities of various sizes and shapes. Our numerical experiments verified and extended, for a class of nonlinear elasticity materials, the theory of Sivaloganathan and Spector on the configurational forces of cavities, as well as justified a crucial hypothesis of the theory on the cavities. Numerical experiments on configurational forces indicate that, in the case of a round reference configuration with radially symmetric stretch on the boundary, the cavitation centered at the origin is the unique energy minimizer. Numerical experiments also reveal an interesting size effect phenomenon: for macro-scale pre-existing-defects, the cavitation process is dominated by the relatively larger pre-existing-defects, and the cavitation tendency of much smaller pre-existing-defects is significantly suppressed.

Keywords and phrases: isoparametric finite element, cavitation, nonlinear elasticity, energy minimization, configurational force

*The research was supported by the Major State Basic Research Projects (2005CB321701), NSFC projects 10871011 and RFDP of China.

†Corresponding author, email: lizp@math.pku.edu.cn

Contents

1 Introduction

Experiments on elastomers have shown that sufficiently large tensile stress can cause appearance of holes that were not previously evident in the material, the phenomenon is known as cavitation in the relevant literature.

There are basically two fundamental theories on the cavitation phenomenon in nonlinear elasticity. One was developed by Gent and Lindley in 1958 [2], known as the deficiency model, in which the phenomenon is explained as the dramatic enlargement of small pre-existing voids caused by local triaxial tensions. The other was established by Ball in 1982 [1], known as the perfect model, in which the cavitations can be created in the originally intact body in such a way that the total stored energy of the elastic body can be most efficiently reduced, in other words, the deformed configuration with properly created cavities can be energetically favorable under certain circumstances.

Sivaloganathan [3] established a relationship between the two models by showing that, with prescribed cavitation points, the deficiency model solution would converge to the perfect model solution, as the diameters of the initial deficiencies approach to zero. The result was later extended to a more general setting [4] and developed into a regularizing domain method [5], which provided a theoretical approach to obtain an approximate cavitation solution to the perfect model from the one to the deficiency model, under the condition that the cavitation points are prescribed.

Since the energetically favorable cavitation point (or points) are generally not known in advance, it is desirable to develop a method to tell whether a given set of prescribed cavitation points are energetically favorable. Aimed at this and inspired by a non-classical force, called configurational force or material force, previously identified within elasticity in dislocations in crystals, fracture mechanics, phase boundaries and especially in the stressed crystal lattice [9], Sivaloganathan and Spector introduced a useful tool, also named as configurational force in 2002 [6], and they showed that, for the standard radially symmetric problem [1] with one prescribed cavity, and under certain hypotheses on the cavitation solution, the configurational force corresponding to the cavitation solution with a prescribed deficiency point always points to the direction of the origin which is proved to be the unique energetically favorable cavitation point of the problem.

It is of great interest to clarify whether the hypotheses Sivaloganathan and Spector assumed on the cavitation solutions actually hold, and more importantly,

whether the idea of the configurational force works in a more general setting. The purpose of the present paper is to explore the cavitation phenomenon by carrying out a numerical study on the deficiency model and the configurational force, and hopefully to shed some new lights on the relevant issues.

The specific problem we consider is to minimize the total energy of the form

$$E(\boldsymbol{u}) = \int_{\Omega_\varepsilon} W(\nabla \boldsymbol{u}(\boldsymbol{x}))d\boldsymbol{x} \tag{1.1}$$

in a set of admissible deformations

$$\mathbb{U} = \left\{\boldsymbol{u} \in W^{1,1}(\Omega_\varepsilon;\mathbb{R}^{\mathrm{d}}) \text{ is a bijection} : \boldsymbol{u}|_{\Gamma_0} = \boldsymbol{u}_0, \ \det \nabla \boldsymbol{u} > 0 \ \text{ a.e}\right\}, \tag{1.2}$$

where in (1.1) $\Omega_\varepsilon \subset \mathbb{R}^d$ $(d = 2, 3)$ is a domain, which we assume is occupied by a nonlinearly elastic body in its reference configuration, of the form

$$\Omega_\varepsilon = \Omega \setminus \bigcup_{i=1}^{n} B_{\varepsilon_i}(\boldsymbol{x}_i),$$

with Ω being a regular defect free domain in $\mathbb{R}^d$ $(d = 2, 3)$ and $B_{\varepsilon_i}(\boldsymbol{x}_i)$ being the pre-existing-defects of diameters ε_i centered at points $\boldsymbol{x}_i$, $i = 1, \ldots, n$, for example in the simplest form we may consider $B_{\varepsilon_i}(\boldsymbol{x}_i) = \{\boldsymbol{x} : |\boldsymbol{x} - \boldsymbol{x}_i| < \varepsilon_i\}$, and where $W : M^{d\times d}_+ \to \mathbb{R}$ is the stored-energy density function and $M^{d\times d}_+$ denotes the real $d \times d$ matrices with positive determinant; and where in (1.2) $\Gamma_0 = \partial\Omega$.

For simplicity, we will restrict ourselves to consider the same polyconvex energy density function as used in [6]

$$W(\boldsymbol{F}) = \kappa|\boldsymbol{F}|^p + \mathrm{h}(\det \boldsymbol{F}), \quad \boldsymbol{F} \in M^{d\times d}_+, \ p \geq 1, \tag{1.3}$$

where $\kappa > 0$ is a material constant, $|\cdot|$ denotes the Euclidean norm ($|\boldsymbol{A}|^2 = \mathrm{trace}(\boldsymbol{A}^{\mathrm{T}}\boldsymbol{A})$), and $\mathrm{h} : (0, \infty) \to [0, \infty)$ is continuously differentiable, convex and satisfies

$$\mathrm{h}(\delta) \to +\infty \text{ as } \delta \to 0, \ \text{ and } \ \frac{\mathrm{h}(\delta)}{\delta} \to +\infty \text{ as } \delta \to +\infty;$$

and to consider a simple expansionary boundary condition on Γ_0, more precisely, we set $\boldsymbol{u}_0 = \lambda\boldsymbol{x}$, where $\lambda > 0$ is a sufficiently large parameter. This leads to the following mixed displacement/traction boundary value problem of the Euler-Lagrange equation:

$$\mathrm{div}(D_F W(\nabla \boldsymbol{u})) = \boldsymbol{0}, \qquad \text{in } \Omega_\varepsilon, \tag{1.4}$$

$$D_F W(\nabla \boldsymbol{u})\,\boldsymbol{\nu} = \boldsymbol{0}, \qquad \text{on } \cup_{i=1}^{N} \Gamma_i, \tag{1.5}$$

$$\boldsymbol{u}(\boldsymbol{x}) = \lambda\boldsymbol{x}, \qquad \text{on } \Gamma_0, \tag{1.6}$$

where $\boldsymbol{\nu}$ denotes the unit exterior normal with respect to Ω_ε, $\Gamma_i = \partial B_{\varepsilon_i}(\boldsymbol{x}_i)$, $i = 1, \cdots, n$, are the boundaries of the pre-existing defects, and where, for the stored energy density function given by (1.3), we have

$$D_F W(\nabla \boldsymbol{u}) = p\kappa \big|\nabla \boldsymbol{u}\big|^{p-2} \nabla \boldsymbol{u} + h'(\det \nabla \boldsymbol{u}) \operatorname{adj} \nabla \boldsymbol{u}^{\mathrm{T}}. \tag{1.7}$$

Now suppose that $\boldsymbol{x}_1 \in \Omega$ is the only possible defect point in Ω, and $\boldsymbol{u}(., \boldsymbol{x}_1, \lambda)$ is the minimizer of E that creates no new holes in $\bar{\Omega} \setminus \{\boldsymbol{x}_1\}$ and which may or may not create a new hole at the prescribed point $\boldsymbol{x}_1$. Results of Eshelby [9, 11] show that the configurational or material force on $\boldsymbol{x}_1$ is given, in particular, by

$$\boldsymbol{f}(\boldsymbol{x}_1, \lambda) := \int_{\partial\Omega} \boldsymbol{M}(\nabla \boldsymbol{u}(\boldsymbol{x}, \boldsymbol{x}_1, \lambda)) \boldsymbol{n}(\boldsymbol{x}) \, \mathrm{d}s, \tag{1.8}$$

where $\boldsymbol{M}(\cdot)$ is the energy-momentum tensor defined by

$$\boldsymbol{M}(\nabla \boldsymbol{u}) = W(\nabla \boldsymbol{u}) \boldsymbol{I} - \nabla \boldsymbol{u}^T \frac{\partial W}{\partial F}(\nabla \boldsymbol{u}).$$

Sivaloganathan and Spector showed in 2002 [6] that, under certain general hypotheses, the configurational force gives the steepest decent direction of the energy E in the sense that the deceasing rate of the energy of the corresponding cavitation solution will reach the maximum, if the unique defect position $\boldsymbol{x}_1$ is moved in this particular direction instead of others.

The cavitation phenomenon, including the cavity nucleation, growth and merge, has long being considered one of the key elements of the underline mechanisms of the fracture initiation and growth in nonlinear elastic materials, and mathematical modeling and numerical simulation have been expected to play a crucial rule in studying the cavitation phenomenon. However, due to its complexity, the analytical and numerical results on the solutions are mostly concentrated on the 1D problem reduced from radially symmetric models (for the numerical studies and the corresponding references see [13] and [14] among many others). To our knowledge, the first and probably the only 2D numerical simulation on cavitation appeared so far in the literature was given by Negrón-Marrero in 1986 [15], where a spectral-finite difference method was applied to a single-prescribed-defect problem.

Not as commonly would have been expected by many researchers, the result on the generally believed versatile finite element methods can be hardly found, if there is any, in the literature of cavitation computations. One of the main reasons that the finite element methods failed so far to successfully simulate the cavitation phenomenon is shown in Figure 1, where it is clearly seen that, when a small ring

undergoes a sufficiently large expansionary deformation, a typical triangular element $\triangle ABC$ of a piecewise affine interpolation of the small ring will deform into $\triangle A'B'C'$ with reversed orientation, and thus the corresponding finite element deformation is not admissible (see (1.2)). In numerical simulations, the phenomenon would either prevent the small deficiency growing into large voids or cause mesh tanglement and produce physically unfeasible interpenetrating numerical solutions. Only until recently, Lian and Li [7] established a dual-parametric finite element method which successfully overcomes this difficulty for the symmetric cavitation problem, Xu and Henao [8] established a penalized non-conforming finite element method which is successfully applied to the computation of multiple cavities with some acceptable sacrifice on the approximation accuracy near the cavities' surface to overcome the instability caused by the nonconformity.

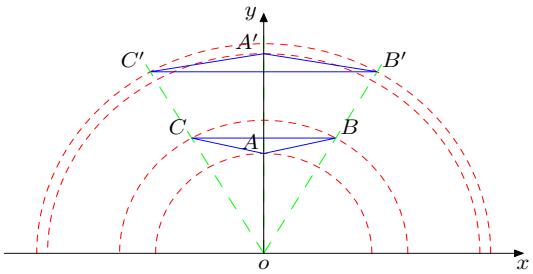

Figure 1: For a sufficiently large expansion of a small ring, the orientation of an affine element can be reversed.

In the present paper, we establish a quadratic iso-parametric finite element method for cavitation problems which allow multiple unsymmetrical prescribed defects of various shapes and sizes, and conduct a series of numerical experiments concerning the convergence of the defect model solutions to the perfect model ones, and the configurational forces corresponding to one or multiple defects. Our numerical experiments show that the quadratic iso-parametric finite element method can very well resolve extremely large expansionary dominant deformations of multiple voids with a reasonably small number of degrees of freedom, and the convergence behavior agrees well with the theoretical result given in [5]. The numerical results also justified the asymptotically circular hypothesis used in [6] for cavitation solutions for a class of materials, and further verified that the configurational forces indeed indicate the directions that the prescribed defects should be moved so that the total energy of the cavitation solution can be most efficiently reduced. Numerical experiments strongly suggest that, for a ball subject to sufficiently large radially symmetric expansionary deformations on the surface, the cavitation solution cen-

tered at the origin is energetically favorable among cavitation solutions with finite number of cavities. We also discovered an interesting size effect phenomenon: the cavitation process is conditionally dominated by larger prescribed defects.

The rest of the paper is organized as follows. In section 2, we introduce our numerical method which is based on the quadratic iso-parametric finite element discretization and Picard iteration. The numerical experiments and results are presented and discussed in section 3. The concluding remarks are made in section 4.

2 Numerical Method

In this section, we first establish a quadratic iso-parametric finite element method which accommodates cavitations, and we will see how amazingly well it works for large expansionary deformations. Then, we discretize the energy minimizing problem described in Section 1, and present an algorithm based on a modified Picard iteration scheme to solve the induced discrete Euler-Lagrange equation.

2.1 A quadratic iso-parametric finite element method

2.1.1 The standard quadratic iso-parametric finite element

Suppose $(\hat{T}, \hat{P}, \hat{\Sigma})$ [12] is a quadratic Lagrange reference element,

$$\begin{cases} \hat{T} \text{ is the reference triangular element shown in Figure 2 (a)}, \\ \hat{P} = P_2(\hat{T}) \text{ is the set of polynomials of order no greater than 2}, \\ \hat{\Sigma} = \{\hat{p}(\hat{a}_i), 1 \le i \le 3;\ \hat{p}(\hat{a}_{ij}), 1 \le i < j \le 3\}, \end{cases} \tag{2.1}$$

where $\hat{a}_i$ denotes the vertexes of the reference triangular element, and $\hat{a}_{ij}$ denotes the midpoint between $\hat{a}_i$ and $\hat{a}_j$.

For a given set of six points $a_i, 1 \le i \le 3$, and $a_{ij}, 1 \le i < j \le 3$ in $\mathbb{R}^2$, define a quadratic mapping $F_T : \hat{T} \to \mathbb{R}^2$ by

$$\begin{cases} F_T \in (P_2(\hat{T}))^2, \\ x = F_T(\hat{x}) = \sum_{i=1}^{3} a_i \hat{\mu}_i(\hat{x}) + \sum_{1 \le i < j \le 3} a_{ij} \hat{\mu}_{ij}(\hat{x}), \end{cases} \tag{2.2}$$

where

$$\hat{\mu}_i(\hat{x}) = \hat{\lambda}_i(\hat{x})(2\hat{\lambda}_i(\hat{x}) - 1),\ \hat{\mu}_{ij}(\hat{x}) = 4\hat{\lambda}_i(\hat{x})\hat{\lambda}_j(\hat{x}),$$

with $\hat{\lambda}_i(\hat{x}), 1 \le i \le 3$ being the barycentric coordinates of $\hat{T}$.

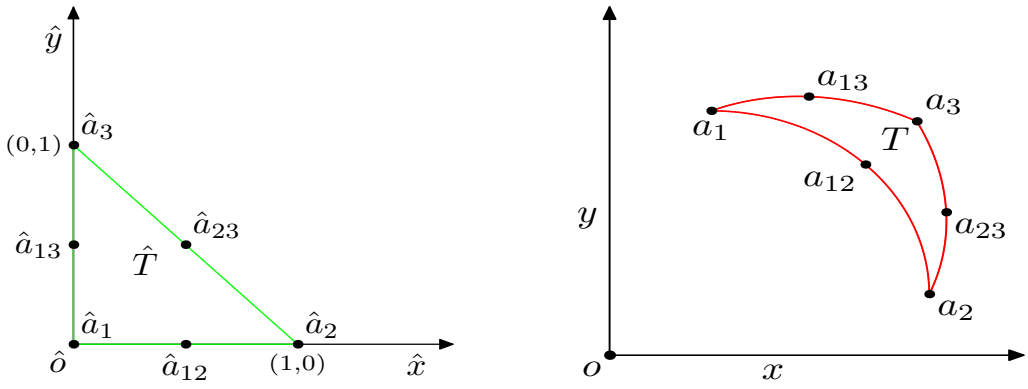

(a) The reference element $\hat{T}$ (b) The curved triangular element T

Figure 2: The standard reference element and typical curved quadratic element.

If F_T is a one-one mapping, then $T = F_T(\hat{T})$ defines a curved triangular element as shown in Figure 2(b).

The standard quadratic iso-parametric finite element is now defined as a finite element triple [12] (T, P_T, Σ_T) with

$$\begin{cases} T = F_T(\hat{T}) \text{ being a curved triangle element,} \\ P_T = \{p : T \to \mathbb{R}^2 \mid p = \hat{p} \circ F_T^{-1},\ \hat{p} \in \hat{P}\}, \\ \Sigma_T = \{p(a_i), 1 \le i \le 3; p(a_{ij}), 1 \le i < j \le 3\}. \end{cases} \tag{2.3}$$

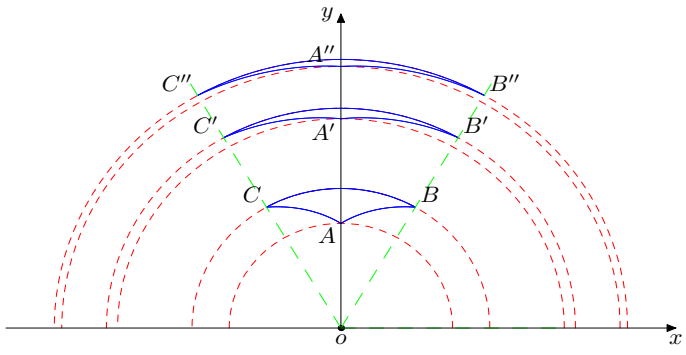

Figure 3: The quadratic iso-parametric finite element admits large orientation preserving expansionary deformations.

As is illustrated in Figure 3, the quadratic iso-parametric finite element permits extremely large orientation preserving expansionary deformations, which we regard as a key feature that a method must have for a successful numerical computation of cavitation problems.

2.1.2 Locally large expansion accommodating curved triangulations

The first step to establish an efficient quadratic iso-parametric finite element method is to introduce cavitation accommodating curved triangulations on the reference domain Ω_ε.

Let $\mathcal{J}$ be a given straight edged triangulation on Ω_ε, let x_k, $k = 1 \dots n$, be the center of the k-th defect whose radius is ε_k, which is assumed to be small. Let $C > 1$ be a given constant, denote $B_{\eta_k}(\boldsymbol{x}_k) = \{\boldsymbol{x} : |\boldsymbol{x} - \boldsymbol{x}_k| < \eta_k\}$ with $\eta_k \geq C\varepsilon_k$ satisfying $B_{\eta_k}(\boldsymbol{x}_k) \cap B_{\eta_l}(\boldsymbol{x}_l) = \emptyset$ if $k \neq l$. For a triangular element $K \in \mathcal{J}$ with vertices $\boldsymbol{a}_i, 1 \leq i \leq 3$, we initially define the middle points as $\boldsymbol{a}_{ij} = (\boldsymbol{a}_i + \boldsymbol{a}_j)/2$, $i \neq j$. Inspired by the dual-parametric finite element method [7], to accommodate the possible extremely large expansionary deformation around the defects, we redefine the middle points in the following way:

- if there exists some k, $1 \leq k \leq n$, such that $\boldsymbol{a}_i$, $\boldsymbol{a}_j \in B_{\eta_k}(\boldsymbol{x}_k)$, denote $(r_k(\boldsymbol{x}), \theta_k(\boldsymbol{x}))$ the local polar coordinates of $\boldsymbol{x}$ with respect to $\boldsymbol{x}_k$, that is $\boldsymbol{x} - \boldsymbol{x}_k = (r_k(\boldsymbol{x}) \cos\theta_k(\boldsymbol{x}), r_k(\boldsymbol{x}) \sin\theta_k(\boldsymbol{x}))$, and redefine the midpoint as

$$\boldsymbol{a}_{ij} = (r_{ij} \cos\theta_{ij}, r_{ij} \sin\theta_{ij}), \tag{2.4}$$

  where

$$r_{ij} = \frac{r_k(\boldsymbol{a}_i) + r_k(\boldsymbol{a}_j)}{2}, \quad \theta_{ij} = \frac{\theta_k(\boldsymbol{a}_i) + \theta_k(\boldsymbol{a}_j)}{2}.$$

Now, the 3 vertices $\boldsymbol{a}_i$ and 3 new middle points $\boldsymbol{a}_{ij}$ will generally define a curved element $\tilde{K}$ corresponding to a quadratic mapping (for example the straight edged triangle $\triangle ABC$ in Figure 1 will be changed to the curved triangle $\tilde{\triangle} ABC$ in Figure 3). The elements on the boundary are adjusted in a standard way to achieve a better approximation of the reference domain Ω_ε.

Briefly speaking, in addition to the standard treatment on the boundary, our triangulation consists of curved triangles particularly defined according to the local polar coordinates on the region near the defects to better accommodate the locally expansion dominant deformations.

2.1.3 Numerical verification of the orientation preserving property

As is mentioned in Section 1, the reverse of orientation under large expansionary deformation is the main reason that causes the failure of the piecewise affine conforming finite element method for the cavitation problem. We will see below

that the quadratic iso-parametric finite element method can be made to preserve orientation under certain easily satisfied conditions on the triangulations.

In the symmetric case, the solution with a single cavity has the following form:

$$\boldsymbol{u}(\boldsymbol{x}) = \frac{r(R)}{R}\boldsymbol{x}, \quad \text{where } R = |\boldsymbol{x}|. \tag{2.5}$$

In particular, if the material is incompressible, which means $r'(R)\frac{r(R)}{R} = 1$, suppose $r(\varepsilon) = c$, where ε is the radius of the initial void and c is the radius of the final cavity, then we have $r(R) = \sqrt{R^2 - \varepsilon^2 + c^2}$.

Figure 4(a) shows a typical curved triangulation around the prescribed circular void with $\varepsilon = 0.01$. There are two types of curved triangles in the triangulation, namely type A and type B specified in Figure 4(a). Since type B triangles are never found to reverse under expansionary deformation, we restrict ourselves to the orientation preserving conditions for type A triangles. For a type A triangle $\triangle ABC$ shown in Figure 3, denote $\varepsilon = |OA|$ the inner radius of the void, denote $\tau = |OC| - |OA|$ the thickness of the circular annulus, and denote $N = 2\pi/\angle COB$ the number of type A triangles in the circular annulus. In Figure 4(a), we have $\varepsilon = 0.01$, $\tau = 0.01$, $N = 16$, and Figure 4(b) shows the corresponding deformed configuration of the cavity solution with $c = 1$. Notice that in general, for a given final cavity size $c \geq 1$, the thickness of the deformed circular annulus with initial thickness $\tau \ll 1$ is no greater than $\tau^2/2$. This implies that, in double machine precision, one can not distinguish the deformed circular annulus if the initial thickness $\tau < 0.5 \times 10^{-7}$.

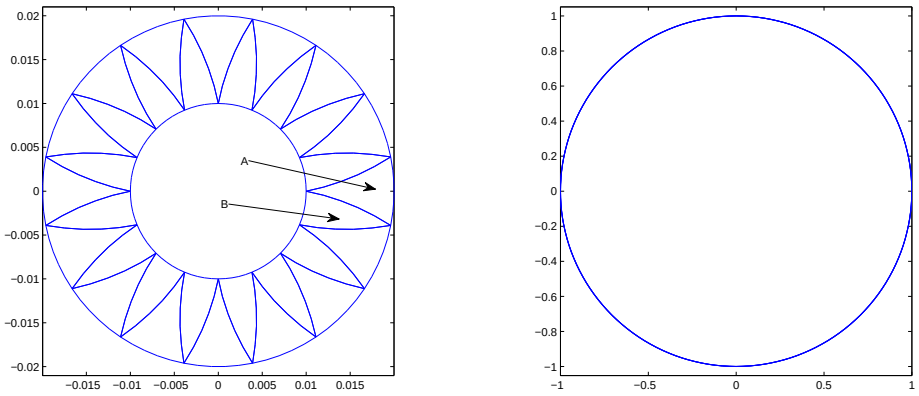

(a) A typical curved triangulation. (b) Cavity solution for $c = 1$.

Figure 4: The quadratic elements around a circular void which grows into a cavity.

To verify that the piecewise quadratic interpolation deformation preserves orientation, we check the positiveness of the Jacobian determinant of the deformation gradient at each of the 12 order Gaussian quadrature points on the type A element. We show in Figure 5(a) that, for any given $\varepsilon > 0$, there is an increasing function $N_\varepsilon(\tau^{-1}) \leq 10\sqrt{\tau^{-1}}$, so that, if $N \geq N_\varepsilon(\tau^{-1})$, in particular, if

$$N \geq 10\sqrt{\tau^{-1}}, \qquad \forall \varepsilon > 0, \tag{2.6}$$

then the corresponding Jacobian determinant of the deformation gradient is positive on every Gaussian quadrature point. For a given $\tau \geq 10^{-7}$, Sharper ε independent lower bounds for N can be found in Figure 5(b).

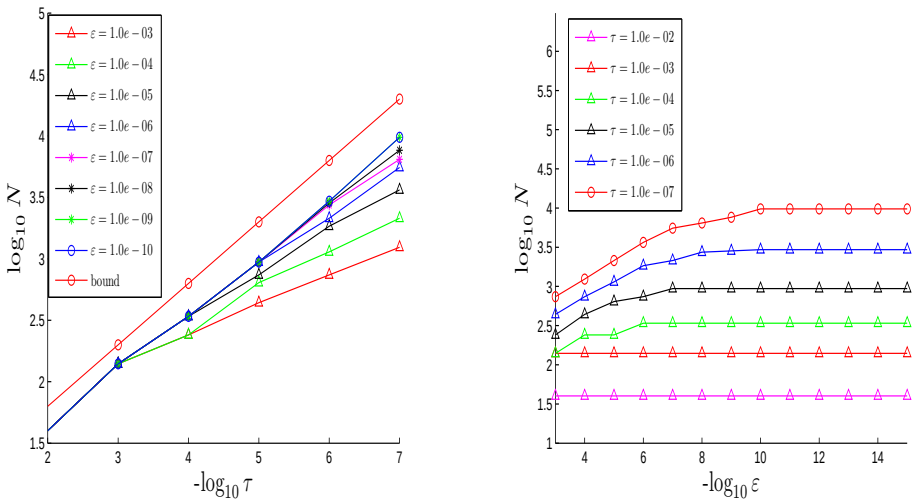

(a) Lower bounds of N for fixed ε. (b) Lower bounds of N for fixed τ.

Figure 5: Bounds of N for orientation preserving cavity interpolation ($c = 1$).

Remark 2.1 *The fact that there exists an ε independent lower bound for N so that the deformation preserves orientation makes it possible for us to control the total degrees of freedom when the prescribed defects are extremely small.*

Remark 2.2 *The lower bounds obtained above are sufficient to guarantee our algorithm to produce reasonably well numerical cavitation solutions. However, further analysis is needed to prove point wise positiveness of the Jacobian determinant of the deformation gradient.*

2.2 The discretization of the problem and the algorithm

Let $\mathcal{J}_h$ be a curved triangulation of the domain Ω_ε with quadratic elements of the form (2.2), and let $\overline{\Omega}_{\varepsilon,h} = \cup_{T\in\mathcal{J}_h} T$. Define the quadratic iso-parametric finite element function space as (see (2.3))

$$X_h := \{\boldsymbol{u}_h \in C(\overline{\Omega}_{\varepsilon,h}) : \boldsymbol{u}_h|_T \in P_T, \boldsymbol{u}_h(\boldsymbol{x}) = \boldsymbol{u}_0(\boldsymbol{x}), \forall \boldsymbol{x} \in \Gamma_0 \cap \partial\Omega_{\varepsilon,h}\}. \tag{2.7}$$

The corresponding homogeneous finite element function space is defined as

$$X_{h,0} := \{\boldsymbol{u_h} \in C(\overline{\Omega}_{\varepsilon,h}) : \boldsymbol{u_h}|_T \in P_T, \boldsymbol{u_h}(\boldsymbol{x}) = 0, \forall \boldsymbol{x} \in \Gamma_0 \cap \partial\Omega_{\varepsilon,h}\}. \tag{2.8}$$

For $\boldsymbol{u_h} \in X_h$, the discrete energy $E_h(\boldsymbol{u}_h)$ may be written in the form

$$E_h(\boldsymbol{u}_h) = \sum_{T\in\mathcal{J}_h} \sum_{j=1}^{M} W(\nabla \boldsymbol{u}_h(b_j))\, \omega_{T,j}, \tag{2.9}$$

where $b_j \in T$, $\omega_{T,j}$, $j = 1, \cdots, M$ are properly chosen quadrature nodes and corresponding quadrature weights. In our numerical experiments, we take $b_j = F_T(\hat{b}_j)$, $\omega_{T,j} = \omega_{\hat{T},j} \det(\nabla F_T(\hat{b}_j))$, where $\hat{b}_j$, $\omega_{\hat{T},j}$ are the quadrature nodes and weights of the 5-th order Gaussian quadrature on the reference element $\hat{T}$. The weak form of the corresponding discrete Euler-Lagrange equation is now read as

$$\sum_{T\in\mathcal{J}_h} \sum_{j=1}^{M} D_F W(\nabla \boldsymbol{u}_h(b_j)) : \nabla \boldsymbol{v}_h(b_j)\, \omega_{T,j} = 0, \quad \forall \boldsymbol{v}_h \in X_{h,0}. \tag{2.10}$$

For the stored energy density function given by (1.3), this gives

$$\sum_{T\in\mathcal{J}_h} \sum_{j=1}^{M} \left[p\kappa|\nabla \boldsymbol{u}_h|^{p-2}\nabla \boldsymbol{u}_h : \nabla \boldsymbol{v}_h + h'(\det \nabla \boldsymbol{u}_h)(\mathrm{adj}\, \nabla \boldsymbol{u}_h)^T : \nabla \boldsymbol{v}_h\right](b_j)\, \omega_{T,j} = 0,$$
$$\forall \boldsymbol{v}_h \in X_{h,0}. \tag{2.11}$$

We apply a modified Picard iteration scheme to solve the discrete Euler-Lagrange equation (2.11), that is to solve the following equation iteratively

$$\sum_{T\in\mathcal{J}_h} \sum_{j=1}^{M} \left[p\kappa|\nabla \boldsymbol{u}_h^n|^{p-2}\nabla(\boldsymbol{u}_h^{n+1} - \boldsymbol{u}_h^n) : \nabla \boldsymbol{v}_h\right](b_j)\, \omega_{T,j} =$$
$$-\triangle t^n \sum_{T\in\mathcal{J}_h} \sum_{j=1}^{M} \left[p\kappa|\nabla \boldsymbol{u}_h^n|^{p-2}\nabla \boldsymbol{u}_h^n : \nabla \boldsymbol{v}_h + h'(\det \nabla \boldsymbol{u}_h^n)(\mathrm{adj}\, \nabla \boldsymbol{u}_h^n)^T : \nabla \boldsymbol{v}_h\right](b_j)\, \omega_{T,j},$$
$$\forall \boldsymbol{v}_h \in X_{h,0}, \tag{2.12}$$

where $\triangle t^n$ is the step size which needs to be properly chosen so that the sequence produced by the iteration is physically admissible and has essentially decreasing total energy. In the computations, the physical admissibility is practically guaranteed by requiring $\det(\nabla \boldsymbol{u}(b_{T,j})) > 0$ for all $1 \le j \le M$ and $T \in \mathcal{J}_h$. The algorithm is summarized as follows.

Algorithm:

(1) Set the initial deformation $\boldsymbol{u}_h^0$ and the initial step size $\triangle t^0$.

(2) Solve the linear finite element equation (2.12) for $(\boldsymbol{u}_h^{n+1} - \boldsymbol{u}_h^n)$ to get $\boldsymbol{u}_h^{n+1}$;

(3) If $\det(\nabla \boldsymbol{u}_h^{n+1})$ is negative on any quadrature node or $E_h(\boldsymbol{u}_h^{n+1}) > E_h(\boldsymbol{u}_h^n)$, then halve the step size $\triangle t^n$ and go to step 2; else, go to step 4.

(4) If $\|\boldsymbol{u}_h^{n+1} - \boldsymbol{u}_h^n\|_{L^2(\Omega_\varepsilon)} < \triangle t^n \cdot \mathrm{TOL}$, then output $\boldsymbol{u}_h^{n+1}$ as the solution and stop; otherwise go to step 2.

Remark 2.3 *Notice that the solution* $(\boldsymbol{u}_h^{n+1} - \boldsymbol{u}_h^n)$ *of the equation* (2.12) *gives the negative gradient direction in the weighted* H^1 *space with the weight* $p\kappa|\nabla \boldsymbol{u}_h^n|^{p-2}$. *This together with* $\det(\nabla \boldsymbol{u}_h^{n+1}) > 0$ *guarantees that the iteration is stable.*

3 Numerical experiments and results

In our 2-D numerical experiments, we use the stored energy density function given in (1.3) with $p = \frac{3}{2}$, $\kappa = \frac{2}{3}$ and $\mathrm{h}(\delta) = \frac{(\delta-1)^2}{2} + \frac{1}{\delta}$, take $\boldsymbol{u}_0 = \lambda \boldsymbol{x}$ (see (1.2) and (2.7)) with the expansionary parameter $\lambda = 2$, and set the X_h interpolation $\boldsymbol{u}_h^0$ of the function $\boldsymbol{u}(\boldsymbol{x}) = \lambda \boldsymbol{x}$ as the initial deformation (see (2.7)).

3.1 Single-defect case

3.1.1 Convergence behavior in the radially symmetric case

To verify the validation of our method, we demonstrate the convergence behavior of our algorithm on a radially symmetric setting where a circular annulus with inner radius ε and outer radius 1 is taken as the reference configuration. It is well known that the problem can be reduced to a 1D minimization problem and the radially symmetric solution can then be obtained numerically with very high precision by using very fine meshes (cf. [16], see also [8], here for the numerical comparison, we use a uniform mesh with 10^8 nodes for the 1D numerical solution).

Figure 6(a) shows the convergence behavior of the numerical cavitation solution obtained by our algorithm on a sequence of nested uniformly refined meshes, where the error is in L^2 norm and N_s is the total degrees of freedom of the quadratic iso-parametric finite element function space. As a comparison, the convergence behavior of the numerical solutions obtained by the Crouzeix-Raviart nonconforming finite element method (see [8]) is also shown in Figure 6(a). Figure 6(b) shows the convergence behavior of the total elastic energy of the numerical cavitation solutions obtained by our algorithm, which in fact reflects also the convergence behavior of the numerical cavitation solutions in $W^{1,p}$ norm and that of the Jacobian determinant in L^1 norm.

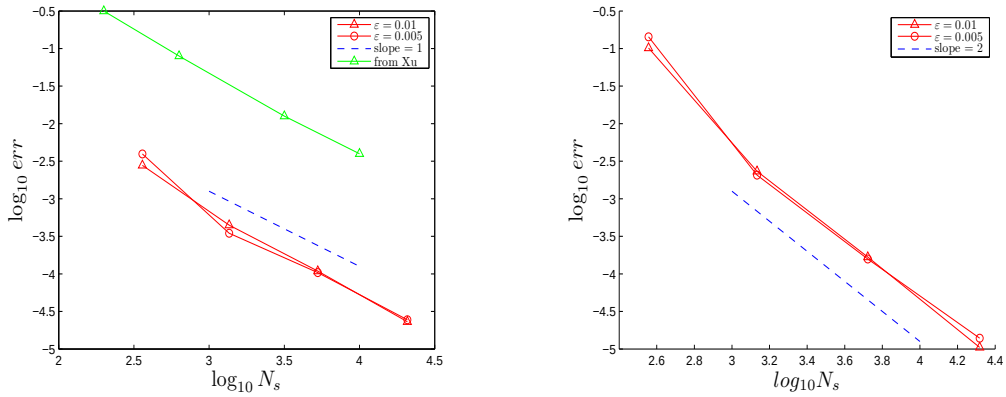

(a) Convergence rate in L^2 norm. (b) Convergence behavior of energy.

Figure 6: The convergence behavior of numerical cavitation solutions ($\lambda = 1.8$).

Remark 3.1 *Intuitively, the excellent performance of our algorithm in the radially symmetric case somehow validates its application to nonsymmetric and multiple defects cases, since in a neighborhood of each prescribed defect the deformation is large expansion dominant, and the global deformation may be viewed as these locally large expansion combined with a globally regular map.*

3.1.2 Initial defect's shape independence of the cavitation

According to the theory established in [5], the cavitation solution $\boldsymbol{u}_\varepsilon$ with a single prescribed initial defect of size ε centered at $\boldsymbol{x}_{1,\varepsilon}$ converges, as $\varepsilon \to 0$, to the cavitation solution $\boldsymbol{u}$ of the perfect model with the prescribed cavity point $\boldsymbol{x}_1 = \lim_{\varepsilon\to 0} \boldsymbol{x}_{1,\varepsilon}$, regardless of the shape of the initial defect. As a consequence, for ε

sufficiently small, we expect to have almost the same numerical results for various shapes of initial defects centered at the same point.

Our numerical experiments match the theory perfectly. In fact, for our numerical examples, where $\boldsymbol{x}_1 = \boldsymbol{x}_{1,\varepsilon} = (0,0)$ and the initial defects are circular, triangular or square in shape respectively as shown in Figure 7, the numerical results for $\varepsilon = 0.1$ are already essentially indistinguishable (see Figure 8).

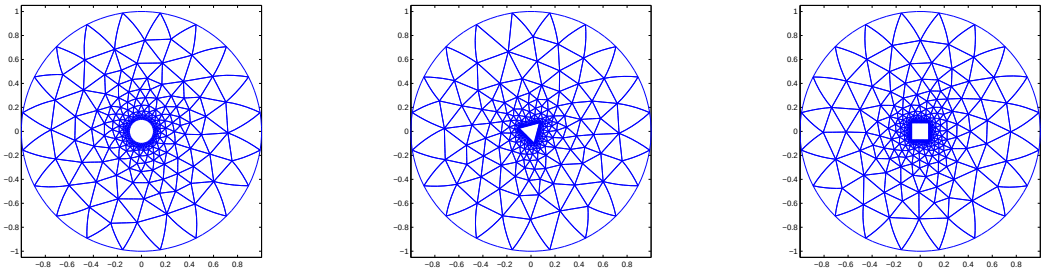

(a) Circular defect (b) Triangular defect (c) Square defect

Figure 7: The meshes for $\overline{\Omega}_{0.1}$ of various shaped defects centered at $(0,0)$.

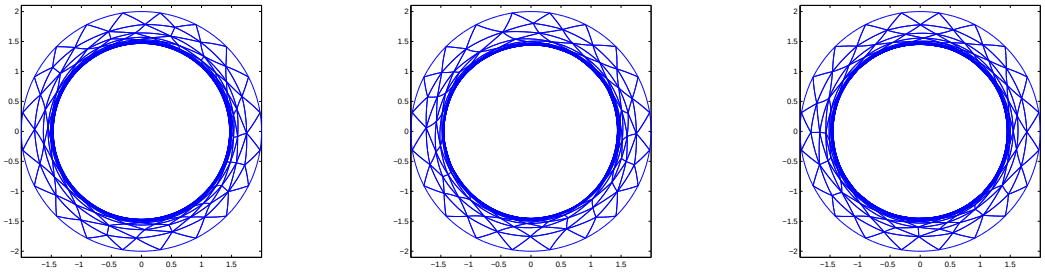

(a) From circular defect (b) From triangular defect (c) From square defect

Figure 8: Numerical cavities growing from various shaped defects centered at $(0,0)$.

The convergence behavior of the algorithm on the above examples with $\varepsilon = 0.1$ is shown in Figure 9(a) and Figure 9(b). We see that, while the convergence with respect to the circular defect is much faster, the limits are shape independent.

Similarly, if we move the center of the defects to $\boldsymbol{x}_1 = \boldsymbol{x}_{1,\varepsilon} = (0.2,0)$, for initial defects of various shapes with $\varepsilon = 0.1$ as shown in Figure 10, we again obtain, as is expected, essentially indistinguishable numerical cavities as shown in Figure 11.

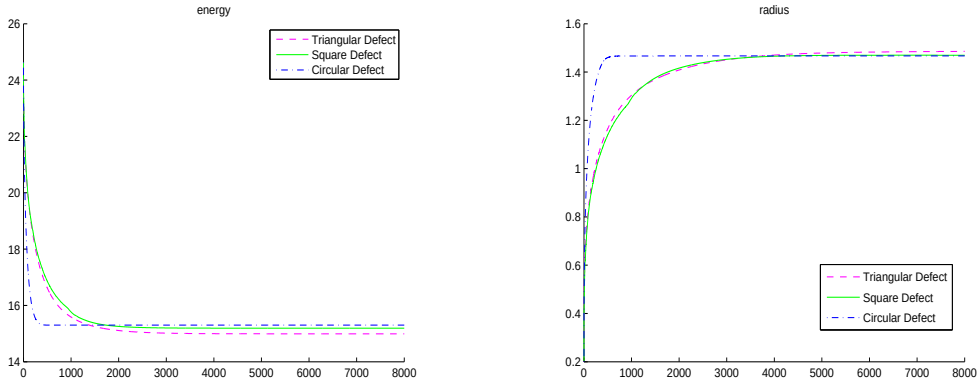

(a) Energy converges decreasingly. (b) Cavity radius converges increasingly.

Figure 9: The convergence behavior of the iteration processes for $\varepsilon = 0.1$.

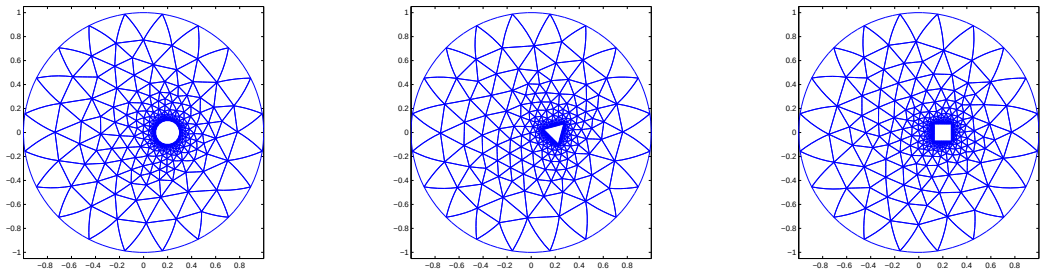

(a) Circular defect (b) Triangular defect (c) Square defect

Figure 10: The meshes for $\overline{\Omega}_{0.1}$ of various shaped defects centered at $(0.2, 0)$.

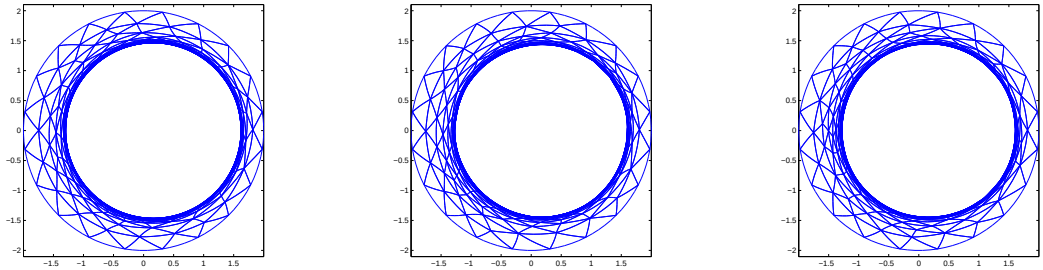

(a) From circular defect (b) From triangular defect (c) From square defect

Figure 11: Numerical cavities growing from various defects centered at $(0.2, 0)$.

3.1.3 Configurational force

Before calculating the configurational force, we would like to check numerically the asymptotically circular hypothesis made in [6] for the cavities, which basically state that the cavities are essentially circular in shape, if possible small variations of scale ε is neglected, regardless of where the prescribed defect is centered.

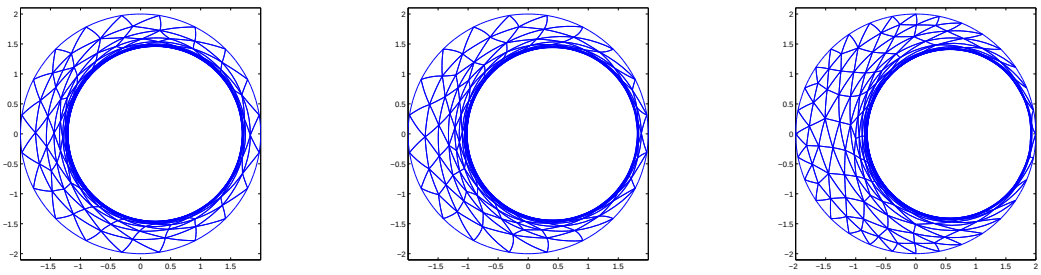

(a) $\boldsymbol{x}_1 = (0.3, 0)$ (b) $\boldsymbol{x}_1 = (0.5, 0)$ (c) $\boldsymbol{x}_1 = (0.7, 0)$

Figure 12: The cavities growing from defects centered at various points.

Notice that the numerical cavities shown in Figure 8 and Figure 11 are almost perfectly circular. More examples are shown in Figure 12, where the almost perfectly circular numerical cavities are created from the prescribed circular defects centered at $\boldsymbol{x}_1 = (0.3, 0), (0.5, 0)$ and $(0.7, 0)$ respectively. The numerical results well justified, at least numerically for the materials used in our example, the asymptotically circular cavity hypothesis used in [6] to prove the geometrical implication of the configurational force pointing to the position of the cavity.

To illustrate the behavior of the numerical configurational force based on the formula (1.8) for the single prescribed defect case, we first set the center of a circular defect of radius 0.1 at $\boldsymbol{x}_1 = (0.5, 0)$, and compute the numerical configurational force on a sequence of refined meshes starting with a coarse mesh of 606 elements as shown in Figure 13(a), where the numerical configurational force obtained is represented by an arrow pointing to the direction of the origin as is predicted by the theory. The convergence behavior of the numerical configurational force is shown in Figure 13(b) and Table 1, where we see that, as the mesh is refined, the x component f_x of $\boldsymbol{f}$ converge to a negative constant $\cong -2.92$, while the y component f_y goes to 0. Table 2 shows the convergence behavior of the numerical configurational forces $\boldsymbol{f}$ and total energy E_{cav} of the cavitation solutions, on meshes with about $600 \sim 700$ elements, corresponding to a single prescribed defect centered at $\boldsymbol{x}_1$ as $\boldsymbol{x}_1 \to 0$. We see that the closer the center $\boldsymbol{x}_1$ to the origin the

smaller the configurational force $\boldsymbol{f}$ and the total energy E_{cav}.

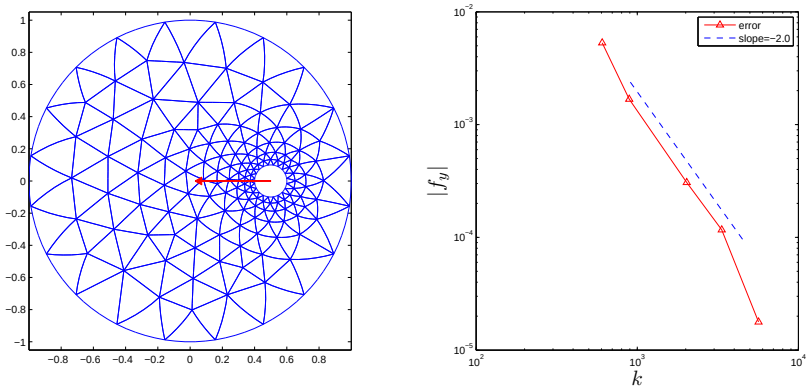

(a) Configurational force on a coarse mesh

(b) Convergence behavior of $|f_y|$

Figure 13: Numerical configurational force $\boldsymbol{f}$ on a 606 elements mesh and the convergence of the y component f_y of $\boldsymbol{f}$ to 0 as the element number $k \to \infty$.

Table 1: Convergence behavior of $\boldsymbol{f}$ as the elements $k \to \infty$.

k	606	892	2028	3346	5660
f_y	-5.3156e-03	-1.6797e-03	-3.0641e-04	1.1648e-04	1.7767e-05
f_x	-2.7976	-2.871	-2.9091	-2.9243	-2.9235

Table 2: Convergence behavior of $\boldsymbol{f}$ and E_{cav} as $\boldsymbol{x}_1$ approaches to the origin.

$\|\boldsymbol{x}_1\|$	0.3	0.2	0.1	0.05	0.01	0.001
E_{cav}	15.51628	15.38884	15.31472	15.29638	15.29071	15.29028
$\|\|\boldsymbol{f}\|\|$	1.4838	0.9711	0.5081	0.2337	0.0516	0.0062

The numerical results shown above agree very well with the theoretical results obtained in [6] for the single-prescribed-defect cavitations, which state:

(i) The configurational force $\boldsymbol{f}(\boldsymbol{x}_1, \lambda)$ is radial, and there is a increasing function $\xi : [0, \infty) \to [0, \infty)$ such that $\boldsymbol{f}(\boldsymbol{x}_1, \lambda) = -\xi(\|\boldsymbol{x}_1\|)\boldsymbol{x}_1$.

(ii) The closer the center of the prescribed defect to the origin the smaller the total energy of the corresponding cavitation solution.

(iii) $\boldsymbol{x}_1 = (0, 0)$ is the unique optimal cavitation point in the sense that the corresponding cavitation solution has the least total energy.

3.2 Multiple-defects case

In this subsection we will see how the idea of the configurational force works for the multiple-prescribed-defects case, and draw conclusions parallel to those of the single-prescribed-defect case, in particular, we will see that the single cavitation solution centered at the origin is most energetically favorable. We will also see that the quadratic iso-parametric finite element works amazingly well for resolving the interactions between the cavities.

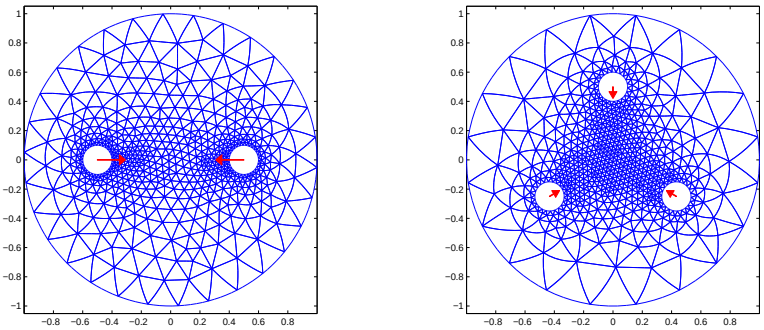

(a) $\boldsymbol{f}_i$ on two prescribed defects (b) $\boldsymbol{f}_i$ on three prescribed defects

Figure 14: Configurational forces on multiple-defects configurations.

Figure 14(a) shows the configurational forces acting upon each defect in a double-prescribed-defects cavitation solution, where the centers of the defects are $\boldsymbol{x}_1 = (0.5, 0), \boldsymbol{x}_2 = (-0.5, 0)$; while Figure 14(b) shows the configurational forces acting upon each defect in a triple-prescribed-defects cavitation solution with the centers of the defects located at $\boldsymbol{x}_1 = (\frac{\sqrt{3}}{10}, -\frac{1}{10}), \boldsymbol{x}_2 = (-\frac{\sqrt{3}}{10}, -\frac{1}{10}), \boldsymbol{x}_3 = (0, \frac{1}{5})$ respectively. We see that in both cases the configurational forces all point to the origin as expected.

Figure 15 shows the convergence behavior of the total energy E of the cavitation solutions corresponding to 1, 2, or 3 prescribed defects as the centers of the defects move symmetrically towards the origin, where $\gamma = \|\boldsymbol{x}_1\| = \|\boldsymbol{x}_2\| = \|\boldsymbol{x}_3\|$ denotes the distance of the defects to the origin. It is clearly shown that in all cases the closer the centers of the defects to the origin the smaller the total energy, which indicates that, as in the single-prescribed-defect case, the configurational force in the multiple-prescribed-defects case also gives the energetically favorable directions to move the defects. In addition, the figure shows that the lowest total energy is achieved by the single cavity as the defect's center approaches the origin.

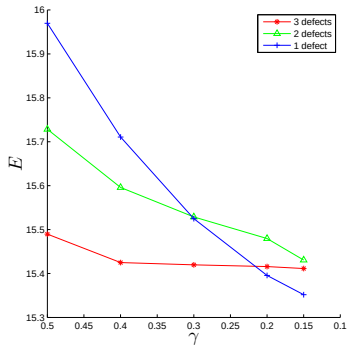

Figure 15: The total energy E decreases monotonically as γ decreases.

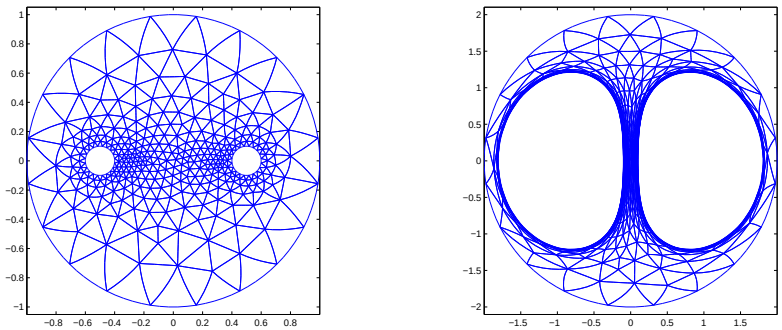

(a) Reference configuration (b) Cavitation solution

Figure 16: Cavitation with 2 defects centered at (-0.5,0) and (0.5,0).

Figure 16 and Figure 17 show, as the two prescribed defects are sufficiently close to each other, the domain between the two defects will be squeezed dramatically in the direction connecting the centers of the defects, while the orthogonal direction will be greatly stretched. Similar numerical results for the 3-prescribed-defects case are shown in Figure 18 and Figure 19. It is interesting to see that, as the defects are getting closer to each other towards the origin, the numerical cavitation solutions look more and more like a cavitation solution growing from a single defect centered at the origin. The numerical results also strongly indicate that, if a fracture mechanism is introduced, the highly squeezed-stretched thin layer between the cavities is most likely to break and the cavities will merge into a single cavity when the prescribed defects are sufficiently close to each other.

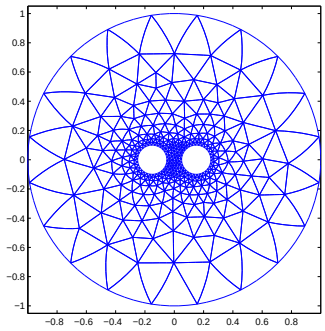
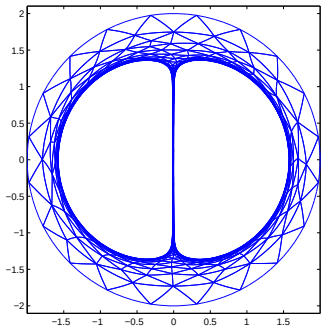

(a) Reference configuration (b) Cavitation solution

Figure 17: Cavitation with 2 defects centered at (-0.15,0) and (0.15,0).

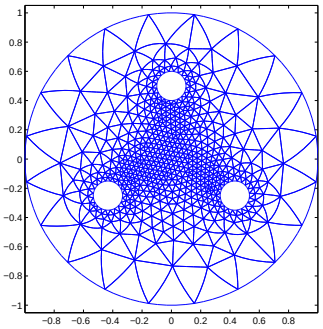
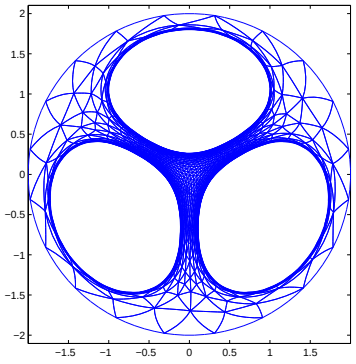

(a) Reference configuration (b) Cavitation solution

Figure 18: Cavitation with 3 symmetrically distributed defects ($\gamma = 0.5$).

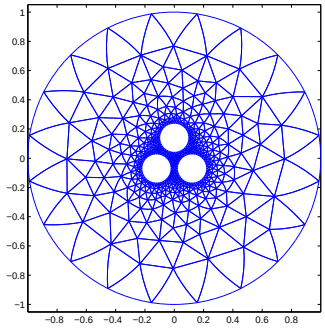
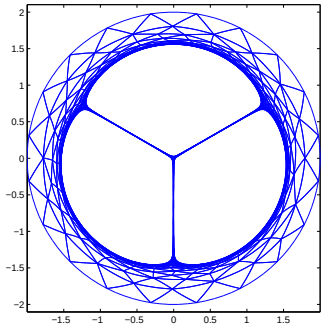

(a) Reference configuration (b) Cavitation solution

Figure 19: Cavitation with 3 symmetrically distributed defects ($\gamma = 0.14$).

3.3 Size effect of the prescribed defects

In this subsection, we present some numerical experiments on cavitations growing from multiple prescribed defects with different sizes and not necessarily symmetrically centered. We will see that a cavity growing from a significantly larger prescribed defect, even if it is centered at an energetically less favorable point, will suppress the growth of smaller defects.

Let $\boldsymbol{x}_1 = (0, 0)$ and $\boldsymbol{x}_2 = (0.3, 0)$ be the centers of two prescribed circular defects. Figure 20 shows the cavitation solution growing from two equally sized defects with $\varepsilon_1 = \varepsilon_2 = 0.02$. We see that the cavity with respect to the defect which is centered at an energetically favorable point is slightly bigger than the other one.

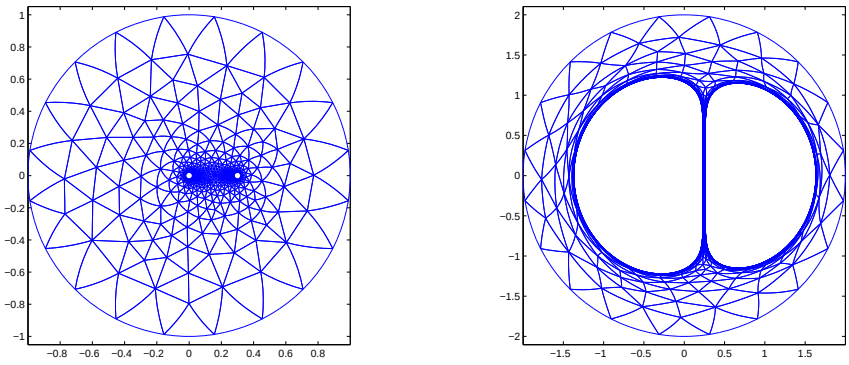

(a) Mesh ($\varepsilon_1 = 0.02$, $\varepsilon_2 = 0.02$) (b) Cavitation solution

Figure 20: Cavities growing from 2 unsymmetrically centered defects of same size.

The numerical cavitation solutions corresponding to two circular prescribed defects with significantly different sizes are shown in Figure 21, where we see the size effect of the prescribed defects, *i.e* the growth of the smaller defects are greatly suppressed by that of the relatively larger ones. Figure 22 and Table 3 illustrate in more quantitative detail the size effect of a cavity growing from a prescribed circular defect centered at $(0.3, 0)$ with radius $\varepsilon_2 = 0.1$, where R_1^{cav} denotes the diameter of the void growing from the circular prescribed defect centered at $(0, 0)$ with radius ε_1. Numerical experiments show that, for the above example, when the size ratio $\varepsilon_2/\varepsilon_1$ is sufficiently large, the smaller defect will not be able to grow into a cavitation solution, instead it will grow into a filamentary shaped void with the stretch ratio, in the direction perpendicular to the line passing through the two defects' centers, approaching to a constant determined completely by the de-

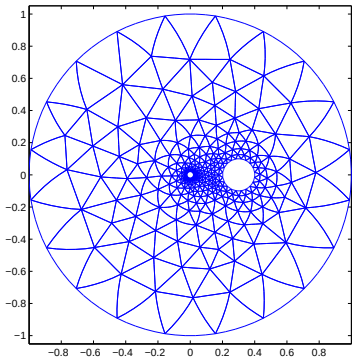

(a) Mesh ($\varepsilon_1 = 0.02$, $\varepsilon_2 = 0.1$)

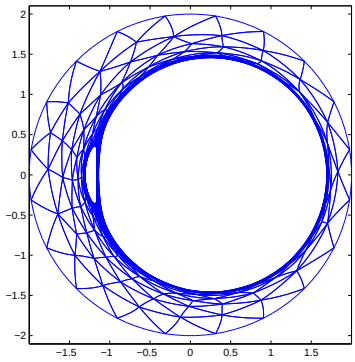

(b) Cavitation solution

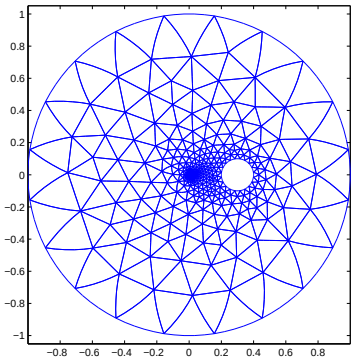

(c) Mesh ($\varepsilon_1 = 0.006$, $\varepsilon_2 = 0.1$)

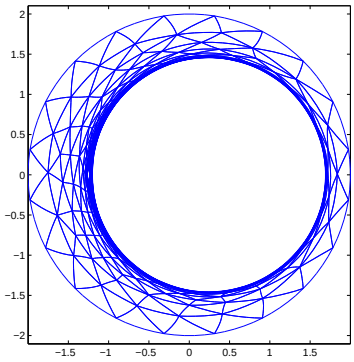

(d) Cavitation solution

Figure 21: Cavities growing from 2 defects of different sizes.

formation caused by the cavitation of the larger defect, in contrast to the situation when the second prescribed defect is absent or is of smaller or comparable size. Figure 23 shows that the closer a smaller defect is to the larger defect the more severely its growth is suppressed.

Table 3: R_1^{cav}/ε_1 converges to a constat as $\varepsilon_1/\varepsilon_2 \to 0$.

ε_1	0.1	0.08	0.06	0.04	0.02
R_1^{cav}	2.787528	2.617787	2.251796	1.552347	7.101325e-01
ε_1	0.008	0.006	0.004	0.002	0.001
R_1^{cav}	2.666570e-01	1.976860e-01	1.288500e-01	6.560967e-02	3.210500e-02

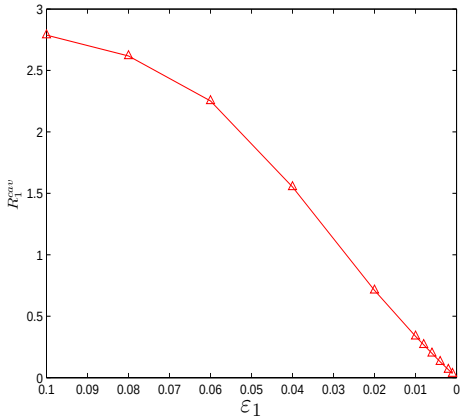

Figure 22: For $\varepsilon_2 = 0.1$ fixed, the diameter $R_1^{cav} \to 0$ as $\varepsilon_1 \to 0$.

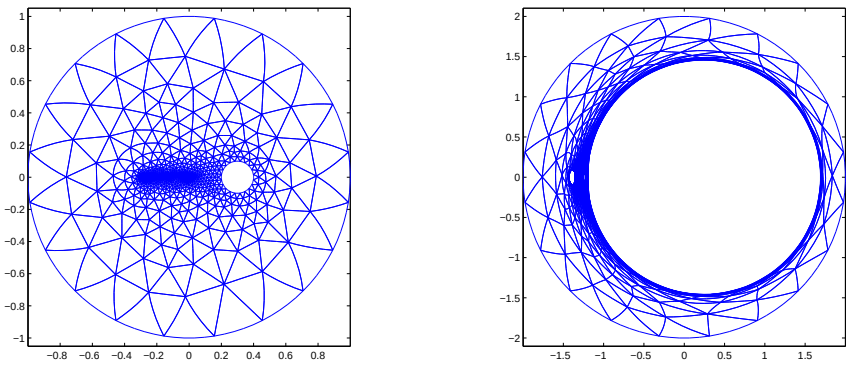

(a) Mesh ($\varepsilon_1 = \varepsilon_2 = 0.005$, $\varepsilon_3 = 0.1$) (b) Cavitation solution

Figure 23: Cavities growing from 3 defects centered at $(-0.3, 0)$, $(0, 0)$ and $(0.3, 0)$.

4 Concluding remarks

A numerical method based on quadratic iso-parametric finite element discretization and a modified Picard iteration scheme is developed in the present paper for the cavitation problem in nonlinear elasticity. The numerical experiments show that the quadratic iso-parametric finite element can well resolve extremely large expansionary dominant deformations and the interactions between cavities. The numerical results not only very well agree with the analytical results on the prescribed-defect's shape independence of the cavitation solution as the size of the defect goes to zero as shown in [5] and on the relationship between the configurational force and the energetically favorable position of a defect for the single-prescribed-defect case obtained in [6], including numerically verified the hypotheses made

there on the cavitation solutions, but also provide sound evidences that some of the corresponding properties can be extended to cavitation solutions with respect to multiple-prescribed-defects. Especially, the numerical results strongly suggest that, in the radially symmetrical initial settings with a circular reference configuration centered at the origin and the radially expansionary boundary displacement $\lambda \boldsymbol{x}$ with sufficiently large λ, the perfect model problem with an energy density of the form (1.3) has a unique energy minimizer among the admissible deformations allowing unsymmetrically distributed and multiple cavitations, which is the cavitation solution with a single cavity centered at the origin. In addition, our numerical experiments revealed an interesting size effect phenomenon, which shows that, in the multiple-prescribed-defects case when the initial sizes of defects are not very small (for our example, $\max_i\{\varepsilon_i\} \geq 0.01$), whether a defect will grow into a cavity depends significantly more on its size than on its position, only significantly larger defects can eventually grow into cavities.

The numerical experiments show that the quadratic iso-parametric finite element method is a powerful tool for computing the cavitations. In particular, since the method can very well resolve the interactions between the cavities, if a proper fracture criteria is introduced, the method can potentially be used to numerically study the merge of cavities, and probably the nucleation and growth of small defects into cracks.

Acknowledgment: The AFEPack is used in our computation for the implement of the iso-parametric finite element, we are grateful to professor Ruo Li of Peking University to help us on the use of the software. We would also like to thank the referees for their valuable comments, which helped a lot to improve the paper.

References

[1] J. Ball, Discontinuous equilibrium solutions and cavitation in nonlinear elasticity, Phil. Trans. Roy. Soc. London. A 306 (1982), 557-611.

[2] A. N. Gent, P. B. Lindley, International rupture of bonded rubber cylinders in tension, Proc. R. Soc. London. A 249 (1958), 195-205.

[3] J. Sivaloganathan, Uniqueness of regular and singular equilibria for spherically symmetric problems of nonlinear elasticity, Arch. Rational Mech. Anal., 96 (1986), 97-136.

[4] J. Sivaloganathan, S. J. Spector, On the existence of minimizers with prescribed singular points in nonlinear elasticity. J. Elasticity, 59 (2000), 83-1113,

[5] J. Sivaloganathan, S. J. Spector, V. Vilakraj, The convergence of regularized minimizers for cavitation problems in nonlinear elasticity, J. Appl. Math 66 (2006), 736-757.

[6] J. Sivaloganathan, S. J. Spector, On cavitation, configurational forces and implications for fracture in a nonlinearly elastic material, J. Elasticity 67 (2002), 25-49.

[7] Yijiang Lian, Zhiping Li, A dual-parametric finite element method for cavitation in nonlinear elasticity, (2010).

[8] Xianmin Xu, D. Henao, An efficient numerical method for cavitation in nonlinear elasticity. To appear in Math. Models Meth. Appl. Sci..

[9] J. D. Eshelby, The force on an elastic singularity. Proc. Roy. Soc. London A 244 (1951), 87-111.

[10] J. D. Eshelby, Energy relations and the energy-momentum tensor in continuum mechanics. In:M. Kanninen, W. Adler, A. Rosenfield, F. Jaffee (eds), Inelastic Behavior of Solid. McGraw-Hill, New York,(1970), 77-115.

[11] J. D. Eshelby, The elastic energy-momentum tensor. J. Elasticity 5 (1975), 321-335.

[12] S. C. Brenner, L. R. Scott, The mathematicl theory of finite element methods, Springer-Verlag, New York, (1994), 67-87.

[13] S. Biwa, Cavitation in finite elasticity with surface energy effects, International Journal of non-linear mechanics, 41 (2006), 1084-1094.

[14] J. Sivaloganathan, P. V. Negrón-Marrero, The numerical computation of the critical boundary displacement for radial cavitation, Mathematics and Mechanics of Solids 14 (2009), 696-726.

[15] P. V. Negrón-Marrero, O. Betancourt, The numerical computation of sigular minimizers in two-dimensional elasticity, J. Comp. Phys. 113 (1994), 291-303.

[16] G. Knowles, Finite element approximation to singular minimizers, and applications to cavitation in nonlinear elasticity, in Differential Equations and Mathematical Physics, Lecture Notes in Math. 1285 (Springer, Berlin, 1987), 236-247.